

# Chapter 1

## Vortex Deformation Close to a Pinning Center

Jun-Yi Ge, Joffre Gutierrez, Valadimir N. Gladilin, Jacques Tempere, Jozef T. Devreese and Victor V. Moshchalkov

### 1.1 Introduction

In type-II superconductors, above the lower critical field  $H_{c1}$ , magnetic field penetrates into the superconductors in the form of quantized vortices with flux  $\Phi_0 = h/2e$  ( $h$ , Plank constant;  $e$ , electron charge), forming the Abrikosov vortex lattice. When a current is applied, the vortices experience a Lorentz force perpendicular to the applied current. Vortex motion under this force leads to energy dissipation that limits technological applications. One common way to solve the problem is by introducing pinning centers to the superconductors, such as lithographically formed well-controlled pinning sites [1–4], ion-irradiated point defects [5], grain boundaries [6], and nanostructured self-assembled non-superconducting phases [7–9]. In all the above cases, the local superconductivity at pinning centers is suppressed, thus making them energetically favorable for vortices to be located on. Therefore, the critical current, above which the dissipation appears due to the vortex motion, can be strongly enhanced.

The vortex–pinning effect has been widely studied by many methods, for example, transport measurements [10–12], ac susceptibility measurements [13–15], and dc magnetization measurements [4, 16, 17]. In the transport measurements, vortices, going through a series of different dynamic regimes [18], are depinned at large enough current density. Theoretical calculations predict that the vortex core becomes elongated along the direction of motion [19]. In the ac susceptibility measurements, under an ac driving force, vortices oscillate around the pinning centers. The interaction between pinning and vortices is manifested a sudden drop of the temperature dependence of in-phase ac susceptibility and a dissipation peak of the

---

J.-Y. Ge · J. Gutierrez · V.N. Gladilin · V.V. Moshchalkov (✉)  
KU Leuven, Celestijnenlaan 200D, 3001 Leuven, Belgium  
e-mail: Victor.Moshchalkov@fys.kuleuven.be

J. Tempere · J.T. Devreese  
Universiteit Antwerpen, Universiteitsplein 1, 2610 Antwerpen, Belgium

out-of-phase ac susceptibility. Various phenomena have been revealed by using ac susceptibility measurement, such as the order–disorder transition and the memory effect of vortex lattice [13]. Isothermal magnetization measurement has also been used to study the vortex–pinning interaction. From the MH curves, the critical current density can be deduced which is directly related to the pinning effect of the superconductor.

However, most of these effects, such as vortex creep [20] and thermally activated flux motion [21], are based on the macroscopic response of the whole vortex lattice to the external drive. At the same time, little attention has been paid to the study of the behavior of an individual vortex when interacting with a pinning potential. A close investigation of this behavior can help us to manipulate vortices at a microscopic level which is important for potential applications such as quantum computing [22] and vortex generators [23]. Using the Ginzburg-Landau (GL) theory, Priour et al. [24] calculated the vortex behavior when approaching a defect. They predicted that a string will develop from the vortex core and extend to the vicinity of the defect boundary, while simultaneously the supercurrents and associated magnetic flux spread out and engulf the pinning center. However, this process happens fast and the vortex will be quickly attracted to the pinning center location, making it extremely hard to access directly with the local probe techniques so far.

Here, we propose a way to solve this problem by using a pair of pinning potentials where one of them traps a vortex. By changing the characteristic lengths,  $\xi$  (coherence length) and  $\lambda$  (penetration depth), simply through varying temperature, we are able to modify the effective interaction between the pinned vortex and the other pinning center nearby. This allows us to directly image the interaction process between a vortex and a pinning center with scanning Hall probe microscopy (SHPM). We have found that, with increasing temperature, the vortex shape becomes elongated with magnetic flux spreading over the adjacent pinning potential, thus providing strong evidence to the “string effect.” The results of theoretical simulations based on the time-dependent Ginzburg-Landau (TDGL) approach are in line with our experimental findings.

## 1.2 Experimental

Our experiment is carried out on a 200-nm-thick superconducting Pb film prepared by ultra-high-vacuum (UHV) e-beam evaporation on a Si/SiO<sub>2</sub> substrate. During the deposition, the substrate is cooled down to liquid nitrogen temperature to avoid the Pb clustering. On top of Pb, 5-nm-thick Ge layer is deposited to protect the sample surface from oxidation. The sample surface is checked by atom-force microscopy (AFM), and a roughness of 0.2 nm is found. The critical temperature  $T_c = 7.3$  K is determined by the local ac susceptibility measurements with a superconducting transition width of 0.05 K, indicating high quality of the sample. The pinning centers in the sample are created during sample preparation, and they appear randomly distributed. The local magnetic-field distribution was mapped using a low-temperature

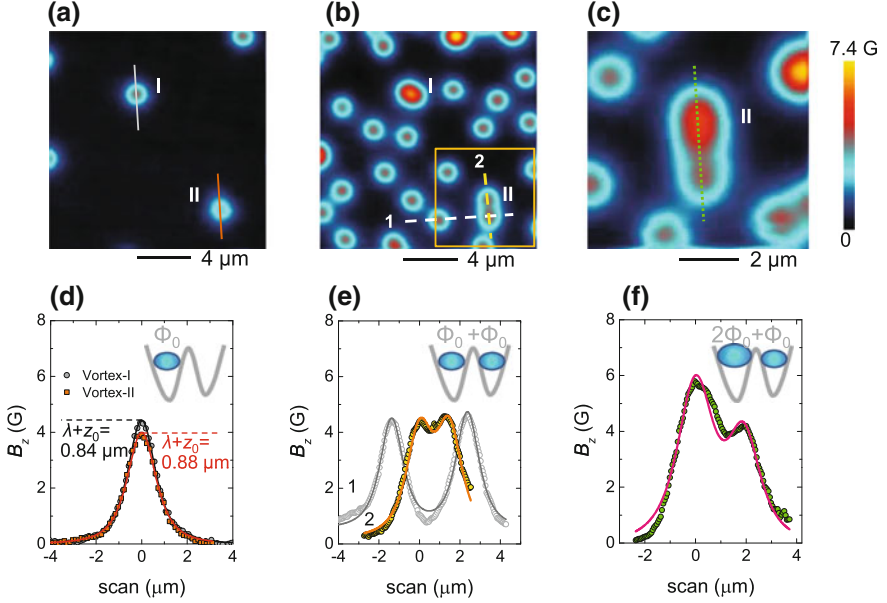


**Fig. 1.1** Distribution of vortices after field cooling, revealing locations of pinning centers. **a–b**: FC images at  $H = 0.3$  Oe **(a)**, 2.4 Oe **(b)** and 3.6 Oe **(c)**. **a** and **b** were taken at the same area, while **c** is taken at the area indicated by the square in **(b)**. At low field **(a)**, only single quantum vortices, sitting on the pinning centers, are observed. At relatively high fields **(b)** and **(c)**, when all the pinning centers are occupied, pinned giant vortices with vorticity  $L = 2$  and interstitial single quantum vortices appear. **d** Field profile along the cross section for the pinned vortices indicated by the *solid lines* in **(a)**. **e** Field profiles along the *dashed lines* as shown in **(b)**. **f** Vortex profile (symbols) along the dotted line in **(c)**. The *solid lines* in panels **d–f** represent fitting of the data with the monopole model. The insets in **d–f** schematically show the pinned vortices at position II, with respect to the pinning landscape

SHPM from Nanomagetics Instruments with a temperature stability better than 1 mK and magnetic-field resolution of 0.1 Oe. All the images are recorded in the lift-off mode by moving the Hall cross above the sample surface at a fixed height of  $\sim 0.7 \mu\text{m}$ . In all the measurements, the magnetic field is applied perpendicular to the sample surface.

### 1.2.1 Distribution of Pinning Centers

Figure 1.1 displays the vortex distributions at  $T = 4.2$  K after field cooling (FC). It is well known that, in the presence of pinning, vortices will nucleate first at the pinning centers as shown in Fig. 1.1a. Two vortices, sitting at positions I and II, are observed in the scanned area. The field profiles for both vortices are displayed in Fig. 1.1d. It is shown that the field strength at the center of the vortex located at position I is higher

than that of vortex sitting at position II. To get quantitative information of confined magnetic flux and penetration depth, the monopole is used [25] with the following expression for the vortex-induced magnetic field:

$$B_z(r, z_0) = \frac{\Phi}{2\pi} \frac{z_0 + \lambda}{\left[r^2 + (z_0 + \lambda)^2\right]^{3/2}} \quad (1.1)$$

where  $\Phi$  is the total flux carried by a vortex,  $\lambda$  is the penetration depth, and  $z_0$  is the distance between effective two-dimensional electron gas (2DEG) of the Hall cross and the sample surface. The distance  $z_0$  is constant in the used lift-off scanning mode. The fitting results are shown by solid lines in Fig. 1.1d, yielding  $\Phi_I = \Phi_{II} = 1.1\Phi_0$ ,  $\lambda_I + z_0 = 0.84 \mu\text{m}$  and  $\lambda_{II} + z_0 = 0.88 \mu\text{m}$ . Since  $\lambda$  is related to the superfluid density,  $\rho_s \propto \lambda^{-2}$  [26], the larger value of  $\lambda_{II} + z_0$ , as compared to  $\lambda_I + z_0$ , suggests a stronger suppression of superconducting condensate at the pinning site where vortex II is located.

The weakened superconductivity at the vortex-II position is further confirmed by the data of FC at a higher field as demonstrated in Fig. 1.1b. At position I, the field pattern in Fig. 1.1b apparently corresponds to a giant vortex with vorticity  $L = 2$ . On the other hand, around position II, two adjacent vortices are observed. The field profiles along the dashed lines in Fig. 1.1b are displayed in Fig. 1.1e. Both of them can be well fitted by two  $\Phi_0$ -vortices located the distance of  $3.7 \mu\text{m}$  (profile (1)) and  $1.27 \mu\text{m}$  (profile (2)) from each other. The fitting results are shown by the solid lines. We also notice that in Fig. 1.1b, the distance between the two vortices located at position II is much smaller than that between interstitial vortices (indicated by the circles in Fig. 1.1b). All these observations suggest that there exist two adjacent pinning sites at the positions II. The pinning potentials of these sites force the two vortices to overcome the vortex–vortex repulsive interaction and stay close to each other. At even higher fields (Fig. 1.1c), one of the two adjacent pinning sites attracts two flux quanta as demonstrated by the field profiles in Fig. 1.1f. This may indicate that its pinning strength is stronger as compared to the bottom located pinning site.

### 1.2.1.1 Vortex Deformation with Temperature

Based on the above estimate of the relative pinning strength, now we focus on the effect of adjacent pinning potentials on a single vortex. To do this, we perform FC at 0.6 Oe to trap one  $\Phi_0$ -vortex (vortex located at position II in Fig. 1.2a). When warming up the sample, both  $\xi(T)$  and  $\lambda(T)$  increase as compared to the temperature-independent distance between the two adjacent pinning sites. In other words, a vortex pinned to one of these sites effectively “approaches” the neighboring site. Each step of this process is imaged directly by SHPM as displayed in Fig. 1.2a–f. For comparison, the field of the vortex located at position I, trapped by an isolated pinning center, is also recorded and analyzed.

At low temperature, both vortices exhibit a circular shape, suggesting the supercurrents are localized about the vortex core. With increasing temperature, the vor-

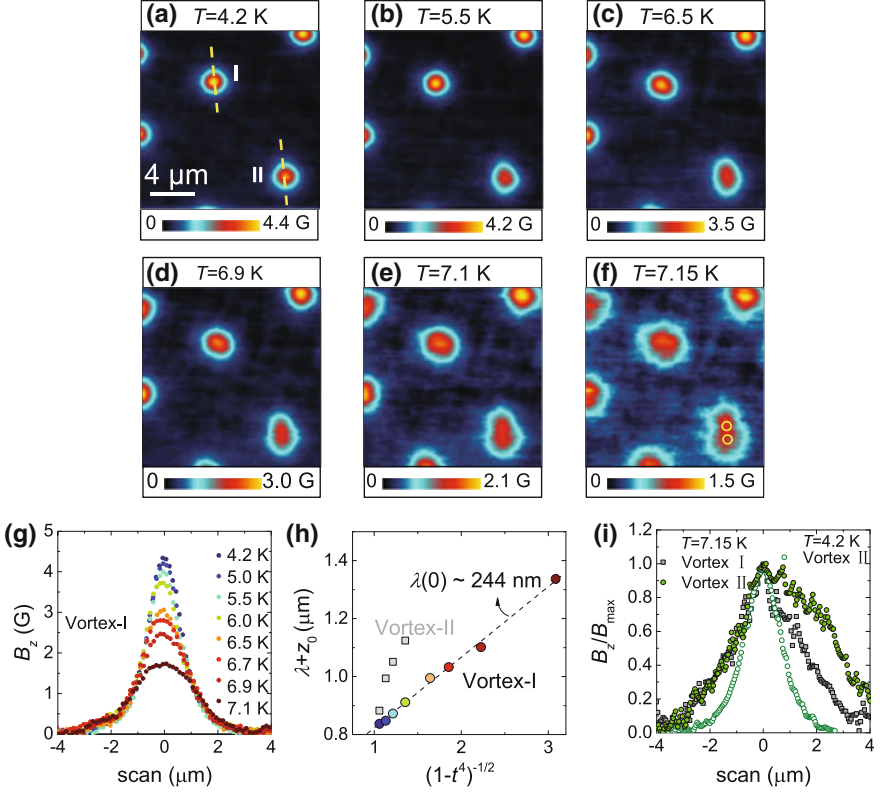


**Fig. 1.2** (Color online) Vortex deformation observed at the pinning centers. **a–f** Scanning Hall probe microscopy images measured after first performing field cooling down to 4.2 K (**a**) and then increasing temperature to 5.5 K **b**, 6.5 K **c**, 6.9 K **d**), 7.1 K **e** and 7.15 K **f**). The circles in **f** indicate the locations where the two  $\Phi_0$ -vortices are pinned in the FC image of Fig. 1.1b. **g** Field profiles of vortex I at different temperatures along the dashed lines indicated in **(a)**. **h**  $\lambda + z_0$  as a function of reduced temperature for vortex I (*squares*) and II (*circles*). The *dashed line* is a linear fit to the data. **(i)** Normalized field profiles for vortex II at 4.2 K (*open circles*) and 7.15 K (*filled circles*). For comparison, the field profile of vortex-I at 7.15 K (*squares*) is also shown

tex at position I preserves its circular shape up to 7.15 K, while the field strength decreases due to the magnetic profile broadening (Fig. 1.2g), correlated with an increase in the penetration depth. By fitting the profiles with the monopole of (1.1), the value of  $\lambda(T) + z_0$  is extracted for different temperatures. According to the two-fluid model [27], in a superconductor with an isotropic energy gap, the temperature dependence of the penetration depth follows the expression  $\lambda(T) = \lambda(0)/\sqrt{1-t^4}$ , where  $\lambda(0)$  is the zero temperature penetration depth and the reduced temperature is  $t = T/T_c$ . As shown by the circles in Fig. 1.2h, for vortex at position I the linear dependence of  $\lambda$  on  $(1-t^4)^{-1/2}$  is obeyed, yielding  $\lambda(0) \approx 244$  nm from the slope. However, the corresponding plot for the vortex located at position II (*squares* in Fig. 1.2h) fails to follow a linear dependence. This is mainly due to a vortex defor-

mation so that the monopole model cannot adequately describe the field distribution. As demonstrated in Figs. 1.2a–f, for vortex at position II, the broadening of the field profile with increasing temperature is asymmetric. As shown in Fig. 1.2i, the vortex field profile becomes elongated in the direction of the line connecting the two adjacent pinning centers (indicated by the open circles in Fig. 1.2f). The fact that this deformation only happens at high temperatures is in agreement with the prediction of [24]: There exists a temperature-dependent critical distance  $d_c$  between a vortex and a pinning center for the “string effect” to happen.

### 1.2.1.2 Simulation Results

To further analyze the observed phenomena, we performed simulations using the time-dependent Ginzburg-Landau (TDGL) equations (see, e.g., [26]). In our model, pinning centers in a superconducting film correspond to reduced local values of the mean free path  $l$ . In the case of inhomogeneous mean free path, the TDGL equation for the order parameter  $\psi$  can be written as follows:

$$\begin{aligned} \left( \frac{\partial}{\partial \tau} + i\varphi \right) \psi &= \frac{l}{l_m} (\nabla - i\mathbf{A})^2 \psi \\ &+ 2(1-t) \left( 1 - \frac{l_m}{l} |\psi|^2 \right) \psi, \end{aligned} \quad (1.2)$$

where  $\varphi$  and  $\mathbf{A}$  are the scalar and vector potentials, respectively, and  $l_m$  is the mean free path value outside the pinning centers. The relevant quantities are made dimensionless by expressing lengths in units of  $\sqrt{2}\xi(0)$ , time in units of  $\pi\hbar/(4k_B T_c) \approx 11.6\tau_{GL}(0)$ , magnetic field in units of  $\Phi_0/(4\pi\xi^2(0)) = H_{c2}(0)/2$ , scalar potential in units of  $2k_B T_c/(\pi e)$ , and  $\psi$  in units of  $|\psi_\infty|$ , the order parameter magnitude far away from pinning centers at  $H = 0$ . Here,  $\mu_0$  is the vacuum permeability,  $\tau_{GL}$  is the Ginzburg-Landau time, and  $\xi(0)$  is the coherence length outside the pinning centers at zero temperature.

The vector potential  $\mathbf{A}$ , for which we choose the gauge  $\nabla \cdot \mathbf{A} = 0$ , can be represented as  $\mathbf{A} = \mathbf{A}_e + \mathbf{A}_s$ . Here,  $\mathbf{A}_e$  denotes the vector potential corresponding to the externally applied magnetic field  $\mathbf{H}$ , while  $\mathbf{A}_s$  describes the magnetic fields induced by the currents  $\mathbf{j}$ , which flow in the superconductor:

$$\mathbf{A}_s(\mathbf{r}) = \frac{1}{2\pi\kappa^2} \int d^3r' \frac{\mathbf{j}(\mathbf{r}')}{|\mathbf{r} - \mathbf{r}'|}, \quad (1.3)$$

where  $\kappa = \lambda/\xi$  is the Ginzburg-Landau parameter and the current density is expressed in units of  $\Phi_0/[2\sqrt{2}\pi\mu_0\lambda(0)^2\xi(0)] = 3\sqrt{3}/(2\sqrt{2})j_c(0)$  with  $j_c$ , the critical (depairing) current density of a thin wire or film [26]. Integration in (1.3) is performed over the volume of the superconductor.

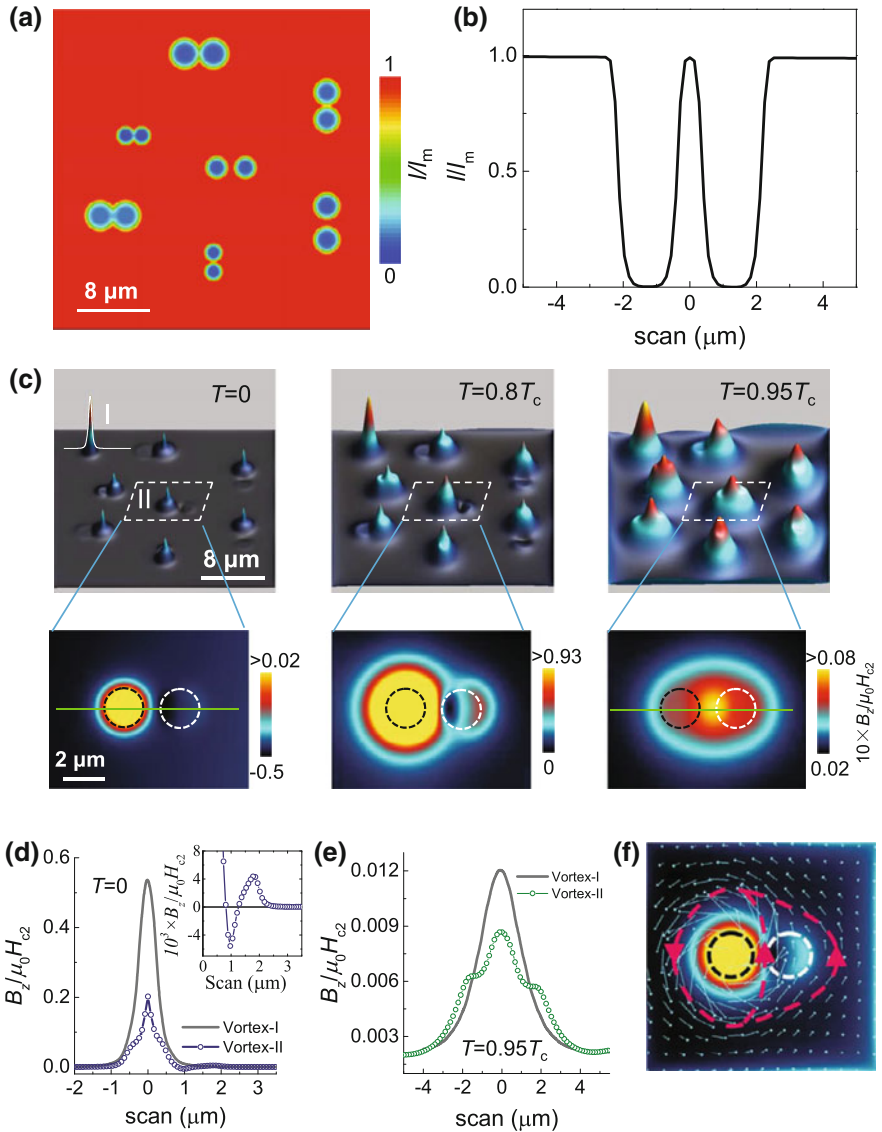


**Fig. 1.3** (Color online) Simulation results. **a** Variations of the normalized mean free path in a  $28 \times 28 \mu\text{m}^2$  superconductor containing seven symmetric pairs of pinning centers with different sizes and strength. **b** Line profile of one pinning pair showing the variation of the normalized mean free path. **c** 3D view of magnetic-field patterns, corresponding to different values of progressively increasing temperature after field cooling to  $T = 0$  at  $H = 0.00375H_{c2}$ . Seven pinned  $\Phi_0$  vortices and one interstitial vortex **i** are observed. The lower panels display an enlarged “top view” of the area indicated by the rectangles in each image. The dashed circles schematically show the pinning centers. The vortex field profiles along the direction of solid lines in **c** at  $T = 0$  and  $0.95T_c$  are given in **(d)** and **(e)**, respectively. The inset in panel **d** provides a close view of the field profile for vortex II in the region between the two pinning centers. **f** Current density vector distribution for a vortex sitting on one pinning center of a pinning pair is indicated by the circles. The red dashed lines and the arrows show schematically the flow of vortex current around the pinning pair

In general, the total current density contains both the superconducting and normal components:  $\mathbf{j} = \mathbf{j}_s + \mathbf{j}_n$  with

$$\mathbf{j}_s = (1 - t) [\text{Im}(\psi^* \nabla \psi) - \mathbf{A} |\psi|^2], \quad (1.4)$$

$$\mathbf{j}_n = -\frac{\sigma}{2} \left( \nabla \varphi + \frac{\partial \mathbf{A}}{\partial t} \right), \quad (1.5)$$

where  $\sigma$  is the normal-state conductivity, which is taken as  $\sigma = 1/12$  in our units [28]. The distribution of the scalar potential  $\varphi$  is determined from the condition

$$\nabla \cdot \mathbf{j} = 0, \quad (1.6)$$

which reflects the continuity of currents in the superconductor. Both  $j_n$  and  $\varphi$  vanish when approaching (meta)stable states, which are of our main interest here.

We assume that the thickness of the superconductor film is sufficiently small, so that variations of the order parameter magnitude across the sample as well as currents in the this direction are negligible and (1.2) becomes effectively two-dimensional. This equation, together with (1.3) and (1.6), is solved self-consistently following the numerical approach described in [29]. Below, we consider a superconducting square with thickness of 200 nm, lateral sizes  $X \times Y = 20 \mu\text{m} \times 20 \mu\text{m}$ ,  $\xi(0) = 210 \text{ nm}$ , and  $\lambda(0) = 160 \text{ nm}$ . As shown in Fig. 1.3A, the pinning sites are introduced as circular areas, where the mean free path  $l$  is smaller than its value  $l_m$  outside pinning centers. These pinning sites are arranged to form seven symmetric ‘‘pinning pairs’’ with different size/depth of pinning centers and distances between them.

The calculated vortex shape evolution with increasing temperature is displayed in Fig. 1.3c. After field cooling down to  $T = 0$ , a  $\Phi_0$  vortex is trapped by one of the pinning centers of each pinning pair. Remarkably, the distribution of the magnetic field, induced by such a pinned vortex, exhibits a tail toward the neighboring pinning center. In contrast, the interstitial vortex, marked as I, remains circularly symmetric up to  $T_c$ . The field distribution in the vicinity of pinned vortex-II at different temperatures is plotted as a color map below each image. The dashed circles indicate the positions of the two pinning centers, which form the pinning pair. At  $T = 0$ , while most of the flux is accumulated around one pinning center (black circle), a ‘‘magnetic-field dipole’’ appears at the position of the other pinning center (white circle). This can also be seen from the magnetic profiles (Fig. 1.3d), which are taken along the solid lines drawn in Fig. 1.3c (for comparison, the vortex profile for vortex-I is also shown). From the inset to Fig. 1.3d, a field dip between the two pinning centers is clearly seen.

The aforementioned magnetic-field dipole is reminiscent of what we have reported for the Meissner state of a superconductor [30]. When the Meissner currents flows through an area containing a pinning center, they generate in its vicinity two opposite sense current half-loops. The magnetic-field pattern, induced by this current configuration, has a dipole-like form (see Fig. 1.4a), which can be considered as a bound



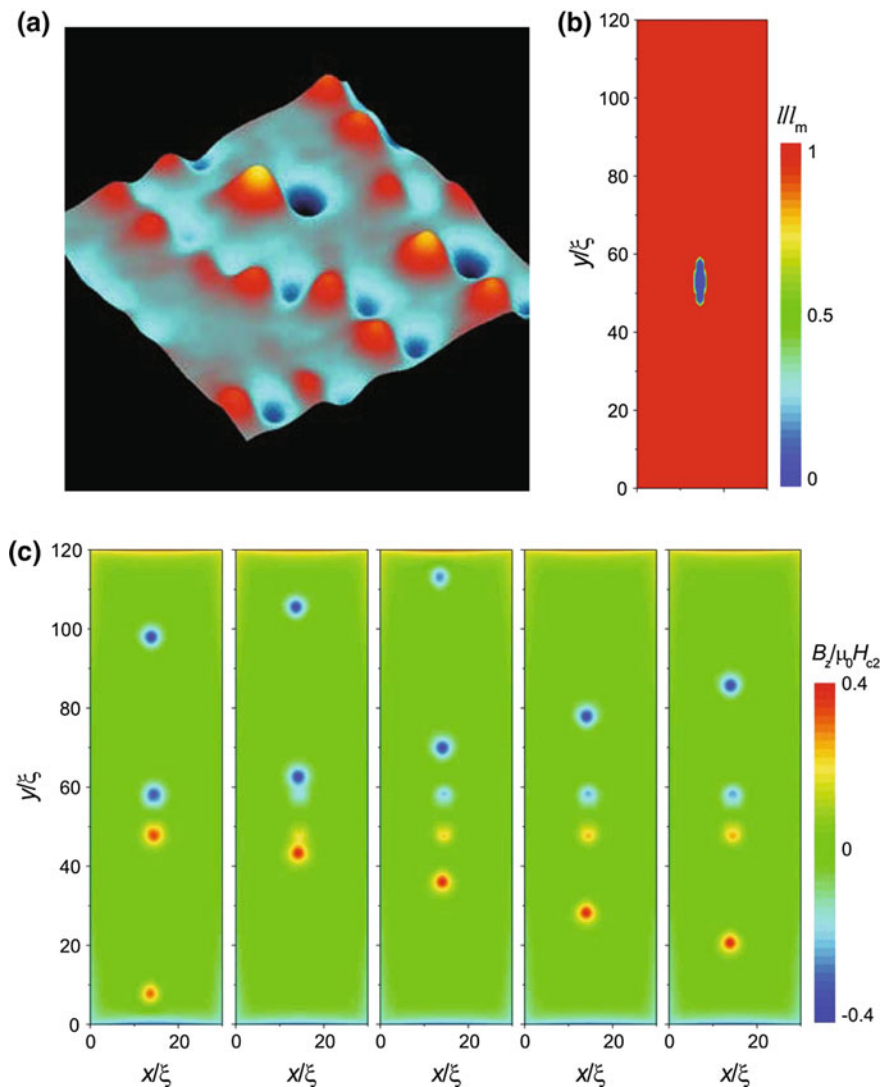


**Fig. 1.4** (Color online) **a** Vortex dipoles observed in the Meissner state of a superconducting Pb film with naturally formed pinning centers. The *bright red* (*dark blue*) color indicates high (*low*) magnetic field. **b** Variations of the mean free path  $l$  assumed for simulation in a superconductor with one pinning center of elongated shape. **c** Simulated magnetic-field distributions for the pinning configuration in B, taken with the time step  $\Delta\tau = 5$ . Single quantum vortices and antivortices are generated from the pinning center at large enough external current ( $j_c = 0.55j_c(T)$ ), applied in the  $x$  direction. The simulations are performed for the penetration depth  $\lambda = \xi$  and the thickness  $d = \xi$ , where  $\xi$  is the coherence length. No external magnetic field is applied

vortex–antivortex pair. Such a bound vortex dipole is qualitatively different from the vortex–antivortex pairs usually observed in the mixed state of a type-II superconductor. Thus, the magnetic flux corresponding to either pole of a vortex dipole is not quantized: It is proportional to the local density of the Meissner currents and hence to the strength of the applied magnetic field. At the same time, our theoretical calculations show that, depending on the size and shape of a pinning center, bound vortex dipoles may evolve into spatially separated vortices and antivortices, if the current density flowing nearby the pinning site is sufficiently high (see Fig. 1.4b and c). In that sense, bound vortex dipoles may be considered as precursors of fully developed vortex–antivortex pairs, in which a vortex (antivortex) carries just one flux quantum. From the point of view of possible applications, measurements of bound vortex dipoles can provide a convenient way to detect hidden submicron defects in superconducting materials in a noninvasive way, which is rather difficult by using a conventional X-ray method.

While in [30] the magnetic-field dipoles are generated by the Meissner current flowing around regions with weakened superconductivity, here the vortex current plays the same role. The origin of the described magnetic-field patterns can be easily understood from Fig. 1.3f, which shows the current density vector distribution for a vortex trapped by one of the sites of the pinning pair. The vortex current extends to engulf both pinning centers of the pair as indicated by the arrows, while between the two pinning centers the current density is reduced. Such a current distribution leads to the formation of a dipole-like pattern of the magnetic field at the location of the unoccupied pinning site.

When increasing temperatures, the circulating currents of the vortex spread over a larger area due to an increase of  $\lambda$ . As a result, the supercurrent flowing around the unoccupied pinning center becomes stronger and the “magnetic-field dipole” signal is enhanced. However, due to the limited resolution of our experimental technique, a negative field signal between the two pinning centers is rather difficult to detect. At even higher temperatures ( $T \geq 0.95T_c$ ), when the vortex core size, which is  $\sim \xi$ , becomes comparable to or larger than the size of the pinning pair as a whole, the thermodynamically stable state corresponds to a vortex centered between the pinning sites (see Fig. 1.3e): Just this position of the vortex provides the maximum overlap of the vortex core with the pinning sites. In this case, the pinning pair acts as a single pinning site with strongly anisotropic shape, which leads to an elongated magnetic-field pattern for the pinned vortex. Similar pinning geometry conversion has also been suggested in Refs. [31, 32]. We have also simulated the vortex deformations in the case of asymmetric pinning pairs, which lead to qualitatively similar results (not shown here).

The vortex distributions at relatively high magnetic fields are shown in Fig. 1.5. At those fields, a pinning center can accommodate more than one vortex. This is consistent with what we have observed in Fig. 1.1b. However, instead of giant vortices, which may be presumed from the experimental data, vortex clusters are formed at pinning sites considered in our theoretical model. This resembles the effect observed in superconducting film with blind antidots, where, due to the large size of blind holes, the trapped  $n\Phi_0$  multiquanta vortex at the antidot dissociates into  $n$  individual

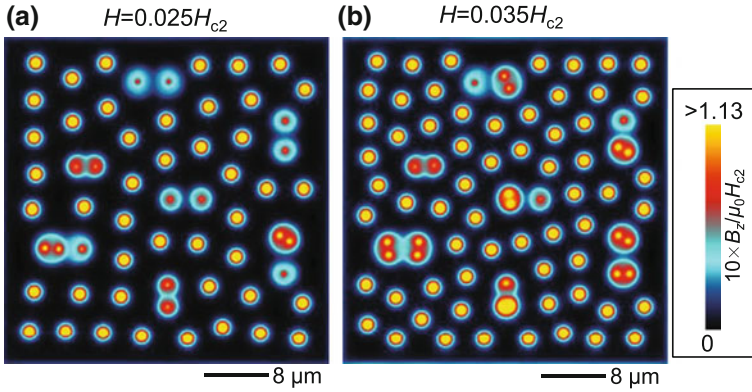


**Fig. 1.5** (Color online) Vortex patterns at relatively high magnetic fields. **a** Vortex patterns, corresponding to FC, for the pinning landscapes of Fig. 1.3a at  $H = 0.025H_c$  **a** and  $0.035H_{c2}$  (**b**)

$\Phi_0$  vortices in the bottom superconducting layer [33]. In this connection, it seems worth mentioning that at present, the resolution of our experimental technique may be not sufficient to confidently distinguish between giant vortices and compact vortex clusters.

To summarize, we have performed both experimental and theoretical studies of vortex states in the vicinity of a pinning center. Our experimental work provides clear evidence of vortex deformation by a nearby pinning center, where the vortex supercurrents and the induced magnetic-field profile expand and engulf the pinning site. The results of our TDGL theoretical modeling, which are fully consistent with the experimental observations, reveal an additional fine structure (“magnetic-field dipoles”) in the magnetic field patterns, induced by those deformed vortices. By simply varying the temperature, the vortex geometry can be well controlled. A detailed understanding of vortex deformation by adjacent pinning centers paves the way to manipulate the vortex current distributions at a microscopic level. This provides new possibilities to control single flux quanta in superconducting devices.

**Acknowledgements** We acknowledge the support from FWO and the Methusalem funding by the Flemish government. This work is also supported by the MP1201 COST action. This research was also supported by the Flemish Research Foundation (FWO-VI), project nrs. G.0115.12N, G.0119.12N, G.0122.12N, G.0429.15N and by the Research Fund of the University of Antwerpen.

## References

1. M. Baert, V.V. Metlushko, R. Jonckheere, V.V. Moshchalkov, Y. Bruynseraede, Composite flux-line lattices stabilized in superconducting films by a regular array of artificial defects. *Phys. Rev. Lett.* **74**, 3269 (1995)

2. V.V. Moshchalkov, M. Baert, V.V. Metlushko, E. Rosseel, M.J. Van Bael, K. Temst, Y. Bruynseraede, R. Jonckheere, Pinning by an antidot lattice The problem of the optimum antidot size. *Phys. Rev. B* **57**, 3615 (1998)
3. N. Haberkorn, B. Maiorov, I.O. Usov, M. Weigand, W. Hirata, S. Miyasaka, S. Tajima, N. Chikumoto, K. Tanabe, L. Civale, Influence of random point defects introduced by proton irradiation on critical current density and vortex dynamics of Ba(Fe<sub>0.925</sub>Co<sub>0.075</sub>)<sub>2</sub>As<sub>2</sub> single crystals. *Phys. Rev. B* **85**, 014522 (2012)
4. D. Ray, C.J. Olson Reichhardt, B. Jank, C. Reichhardt, Strongly enhanced pinning of magnetic vortices in type-II superconductors by conformal crystal arrays. *Phys. Rev. Lett.* **110**, 267001 (2013)
5. B.M. Vlcek, H.K. Viswanathan, M.C. Frischherz, S. Flesher, K. Vandervoort, J. Downey, U. Welp, M.A. Kirk, G.W. Crabtree, Role of point defects and their clusters for flux pinning as determined from irradiation and annealing experiments in YBa<sub>2</sub>Cu<sub>3</sub>O<sub>7- $\delta$</sub>  single crystals. *Phys. Rev. B* **48**, 4067 (1993)
6. C.-L. Song, Y.-L. Wang, Y.-P. Jiang, L. Wang, K. He, X. Chen, J.E. Hokman, X.-C. Ma, Q.-K. Xue, Suppression of Superconductivity by Twin Boundaries in FeSe. *Phys. Rev. Lett.* **109**, 137004 (2012)
7. J.L. MacManus-Driscoll, S.R. Foltyn, Q.X. Jia, H. Wang, A. Serquis, L. Civale, B. Maiorov, M.E. Hawley, M.P. Maley, D.E. Peterson, Strongly enhanced current densities in superconducting coated conductors of YBa<sub>2</sub>Cu<sub>3</sub>O<sub>7- $x$</sub>  + BaZrO<sub>3</sub>. *Nat. Mater.* **3**, 439–443 (2004)
8. J. Gutierrez, A. Llodes, J. Gazquez, M. Gibert, N. Roma, S. Ricart, A. Pomar, F. Sandi-umenge, N. Mestres, T. Puig, X. Obradors, Strong isotropic flux pinning in solution-derived YBa<sub>2</sub>Cu<sub>3</sub>O<sub>7- $x$</sub>  nanocomposite superconductor films. *Nat. Mater.* **6**, 367–373 (2007)
9. S.R. Foltyn, L. Civale, J.L. MacManus-Driscoll, Q.X. Jia, B. Maiorov, H. Wang, M. Maley, Materials science challenges for high-temperature superconducting wire. *Nat. Mater.* **6**, 631–642 (2007)
10. J. Ge, S. Cao, S. Shen, S. Yuan, B. Kang, J. Zhang, Superconducting properties of highly oriented Fe 1.03 Te 0.55 Se 0.45 with excess Fe. *Solid State Commun.* **150**, 1641 (2010)
11. D.B. Rosenstein, I. Shapiro, B.Y. Shapiro, HTransport current carrying superconducting film with periodic pinning array under strong magnetic fields. *Phys. Rev. B* **83**, 064512 (2011)
12. I. Sochnikov, A. Shaulov, Y. Yeshurun, G. Logvenov, I. Bozovic, Large oscillations of the magnetoresistance in nanopatterned high-temperature superconducting films. *Nat. Nanotech.* **5**, 516C519 (2010)
13. J. Ge, J. Gutierrez, J. Li, J. Yuan, H.-B. Wang, K. Yamaura, E. Takayama-Muromachi, V.V. Moshchalkov, Peak effect in optimally doped p-type single-crystal Ba<sub>0.5</sub>K<sub>0.5</sub>Fe<sub>2</sub>As<sub>2</sub> studied by ac magnetization measurements. *Phys. Rev. B* **88**, 144505 (2013)
14. J. Ge, J. Gutierrez, M. Li, J. Zhang, V.V. Moshchalkov, Vortex phase transition and isotropic flux dynamics in K<sub>0.8</sub>Fe<sub>2</sub>Se<sub>2</sub> single crystal lightly doped with Mn. *Appl. Phys. Lett.* **103**, 052602 (2013)
15. J. Ge, J. Gutierrez, J. Li, J. Yuan, H.-B. Wang, K. Yamaura, E. Takayama-Muromachi, V.V. Moshchalkov, Dependence of the flux-creep activation energy on current density and magnetic field for a Ca<sub>10</sub>(Pt<sub>3</sub>As<sub>8</sub>)[(Fe<sub>1- $x$</sub> Pt <sub>$x$</sub> )<sub>2</sub>As<sub>2</sub>]<sub>3</sub> single crystal. *Appl. Phys. Lett.* **104**, 112603 (2014)
16. Y.L. Wang, X.L. Wu, C.-C. Chen, C.M. Lieber, Enhancement of the critical current density in single-crystal Bi<sub>2</sub>Sr<sub>2</sub>CaCu<sub>2</sub>O<sub>8</sub> superconductors by chemically induced disorder. *Proc. Natl. Acad. Sci. USA* **87**, 7058–7060 (1990)
17. M. Motta, F. Colauto, W. Ortiz, J. Fritzsche, J. Cuppens, W. Gillijns, V. Moshchalkov, T. Johansen, A. Sanchez, A. Silhanek, Enhanced pinning in superconducting thin films with graded pinning landscapes. *Appl. Phys. Lett.* **102**, 212601 (2013)
18. J. Gutierrez, A.V. Silhanek, J. Van de Vondel, W. Gillijns, V.V. Moshchalkov, Transition from turbulent to nearly laminar vortex flow in superconductors with periodic pinning. *Phys. Rev. B* **80**, 104514 (2009)
19. D.Y. Vodolazov, F.M. Peeters, Rearrangement of the vortex lattice due to instabilities of vortex flow. *Phys. Rev. B* **76**, 014521 (2007)

20. T. Klein, H. Grasland, H. Cercellier, P. Toulemonde, C. Marcenat, Vortex creep down to 0.3 K in superconducting Fe(Te, Se) single crystals. *Phys. Rev. B* **89**, 014514 (2014)
21. L. Jiao, Y. Kohama, J.L. Zhang, H.D. Wang, B. Maiorov, F.F. Balakirev, Y. Chen, L.N. Wang, T. Shang, M.H. Fang, H.Q. Yuan, Upper critical field and thermally activated flux flow in single-crystalline  $\text{Tl}_{0.58}\text{Rb}_{0.42}\text{Fe}_{1.72}\text{Se}_2$ . *Phys. Rev. B* **85**, 064513 (2012)
22. O. Romero-Isart, C. Navau, A. Sanchez, P. Zoller, J.I. Cirac, Superconducting vortex lattices for ultracold atoms. *Phys. Rev. Lett.* **111**, 145304 (2013)
23. V.M. Fomin, R.O. Rezaev, O.G. Schmidt, Tunable generation of correlated vortices in open superconductor tubes. *Nano Lett.* **12**, 1282 (2012)
24. D. Priour Jr., H. Fertig, Deformation and depinning of superconducting vortices from artificial defects: a Ginzburg-Landau study. *Phys. Rev. B* **67**, 054504 (2003)
25. J. Ge, J. Gutierrez, J. Cuppens, V.V. Moshchalkov, Observation of single flux quantum vortices in the intermediate state of a type-I superconducting film. *Phys. Rev. B* **88**, 174503 (2013)
26. M. Tinkham, *Introduction to Superconductivity* (McGraw-Hill Inc, New York, 1996)
27. J. Bardeen, Two-fluid model of superconductivity. *Phys. Rev. Lett.* **1**, 399 (1958)
28. R. Kato, Y. Enomoto, S. Maekawa, Computer simulations of dynamics of flux lines in type-II superconductors. *Phys. Rev. B* **44**, 6916 (1991)
29. A.V. Silhanek, V.N. Gladilin, J. Van de Vondel, B. Raes, G.W. Ataklti, W. Gillijns, J. Tempere, J.T. Devreese, V.V. Moshchalkov, Local probing of the vortex-antivortex dynamics in superconductor/ferromagnet hybrid structures. *Supercond. Sci. Technol.* **24**, 024007 (2011)
30. J. Ge, J. Gutierrez, V.N. Gladilin, J.T. Devereese, V.V. Moshchalkov, Bound vortex dipoles generated at pinning centres by Meissner current. *Nat. Commun.* **6**, 6573 (2015)
31. J. Trastoy, M. Malnou, C. Ulysse, R. Bernard, N. Bergeal, G. Faini, J. Leseur, J. Briatico, J.E. Villegas, Freezing and thawing of artificial ice by thermal switching of geometric frustration in magnetic flux lattices. *Nat. Nanotech.* **9**, 710–715 (2014)
32. M.L. Latimer, G.R. Berdiyrov, Z.L. Xiao, F.M. Peeters, W.K. Kwok, Realization of artificial Ice systems for magnetic vortices in a superconducting MoGe thin film with patterned nanostructures. *Phys. Rev. Lett.* **111**, 067001 (2013)
33. A. Bezryadin, Y.N. Ovchinnikov, B. Pannetier, Nucleation of vortices inside open and blind microholes. *Phys. Rev. B* **53**, 8553 (1996)